

Physical properties of circumnuclear ionising clusters III. Kinematics of gas and stars in NGC 7742

S. Zamora^{1,2,*}, A. I. Díaz^{1,2}, Roberto Terlevich^{3,4,5}, Elena Terlevich^{3,5}, and R. Amorín^{6,7}

¹ Departamento de Física Teórica, Universidad Autónoma de Madrid, 28049 Madrid, Spain

² CIAFF, Universidad Autónoma de Madrid, 28049 Madrid, Spain

³ Instituto de Astrofísica, Óptica y Electrónica, 72840 Puebla, México

⁴ Institute of Astronomy, University of Cambridge, Madingley Road, Cambridge, UK

⁵ Facultad de Astronomía y Geofísica, Universidad de La Plata, La Plata, Argentina

⁶ Instituto de Investigación Multidisciplinar en Ciencia y Tecnología, Universidad de La Serena, La Serena, Chile.

⁷ Departamento de Astronomía, Universidad de La Serena, La Serena, Chile.

ABSTRACT

Aims. For this third paper in the series, we studied the kinematics of the ionised gas and stars, and calculated the dynamical masses of the circumnuclear star-forming regions in the ring of the face-on spiral NGC 7742.

Methods. We used high spectral resolution data from the MEGARA instrument mounted on the Gran Telescopio Canarias (GTC) to measure the kinematical components of the nebular emission lines of selected HII regions and the stellar velocity dispersions from the CaT absorption lines that allow the derivation of the associated cluster virialised masses.

Results. The emission line profiles show two different kinematical components: a narrow one with a velocity dispersion of ~ 10 km/s and a broad one with a velocity dispersion similar to the values found for the stellar absorption lines. The derived star cluster dynamical masses range from 2.5×10^6 to $10.0 \times 10^7 M_{\odot}$.

Conclusions. The comparison of gas and stellar velocity dispersions suggests a scenario where the clusters have formed simultaneously in a first star formation episode with a fraction of the stellar evolution feedback remaining trapped in the cluster, subject to the same gravitational potential as the cluster stars. Between 0.15 and 7.07 % of the total dynamical mass of the cluster would have cooled down and formed a new, younger, population of stars, responsible for the ionisation of the gas currently observed.

Key words. ISM: abundances – ISM: H II regions – galaxies: ISM – galaxies: starburst – galaxies: star clusters – galaxies: star formation

1. Introduction

Observations of central regions have revealed that nuclear rings are present in at least 20 % of spiral galaxies, with this percentage increasing in galaxies hosting an active galactic nucleus (AGN) (see Knapen 2005). These structures, typically with diameters of hundreds of parsecs, exhibit high star formation rates that have been studied by several authors over the past decades across different wavelengths (e.g. Levy et al. 2022; Lopez et al. 2023; Brandl et al. 2012; Böker et al. 2008; Mazzuca et al. 2008). These star-forming regions, often referred to as hotspots or circumnuclear star-forming regions (CNSFRs), are similar to luminous and large disk HII regions, but look more compact and show higher peak surface brightness (Kennicutt et al. 1989). In early-type spirals they are expected to be of higher metallicity as it corresponds to their position near the galactic bulge (Díaz et al. 2007). In many cases, CNSFRs contribute substantially to the emission of the entire nuclear region seen in the presence of an active nucleus. Their high $H\alpha$ luminosities, typically higher than 10^{39} erg s⁻¹, overlap with those of HII galaxies, and point to relatively massive star clusters as their ionisation source. Hence, these regions are excellent places to study how star formation proceeds in circumnuclear environments; they are crucial for un-

derstanding the connection between nuclear activity and the star formation processes occurring in these hostile environments (see Sarzi et al. 2007).

In previous works, Hägele et al. (2007, 2009, 2010) analysed long-slit high spectral resolution data of CNSFRs in three nearby galaxies: NGC 3351, NGC 2903, and NGC 3310. They used the 4.2m *William Herschel* Telescope (WHT) and the ISIS spectrograph in the blue and red configurations, which provides a comparable velocity resolution of about 13 km/s in both spectral ranges. The $H\beta$ and $[OIII]\lambda 5007$ Å emission lines and the CaII triplet lines (CaT) were present in the spectra, thus allowing the measurement of the gas and star velocity dispersions, which, together with their sizes measured on the WPC2-HST camera and assuming virialisation, made possible the derivation of the dynamical masses of the young clusters in the regions. These masses, found to be between 4.9×10^6 and $1.9 \times 10^8 M_{\odot}$, seem to be rather high and suggest star-forming complexes rather than individual clusters. However, the masses of the corresponding ionising clusters, as derived from $H\alpha$ luminosities under the assumption of no photon escape, only accounts for between 1 % and 10 % of the derived dynamical mass, which raises the question of the possible presence of more than one stellar population in these massive circumnuclear star clusters.

On the other hand, one of the main results of these works shows that for the three observed galaxies, the gas velocity disper-

* PhD fellow of Ministerio de Educación y Ciencia, Spain, BES-2017-080509, CEAL-AL/2017-02

sions as measured from hydrogen recombination lines ($H\beta$ and Paschen emission lines) are found to be considerably smaller (by about 25 km/s) than those measured from the stellar CaT lines. In turn, the velocity dispersion obtained from the $[OIII]\lambda 5007 \text{ \AA}$ line is very close to the measured stellar value. This result suggests the possible existence of two kinematically distinct components in the gas in all regions, although not all of them are associated with the ionising clusters (see Hägele et al. 2013).

The best possibility to resolve this question is to gather observations with both high spatial and spectral resolution simultaneously. At present, the ideal instrument for this is MEGARA, a high-resolution integral field spectrograph (IFS) installed on the 10.4m GTC telescope, covering a field of view (FoV) of $12.5 \times 11.3 \text{ arcsec}^2$ with a spatial resolution of 0.62 arcsec and a spectral range from 3650 to 9700 \AA at three different resolutions, $R \sim 6000, 12000, \text{ and } 20000$. The MEGARA spatial and spectral resolution characteristics ensure the proper identification and resolution of the ionising clusters present in CNSFRs so that the derived masses obtained can be meaningful and reliable.

In the first paper of this series we analyse CNSFRs in the galaxy NGC 7742 using IFS data obtained with the MUSE spectrograph, which provides spectral resolutions between $R \sim 1770 - 3590$ at 4800 and 9300 \AA , respectively. This galaxy is classified as an SA(r)b galaxy and its morphology is dominated by a circumnuclear ring located at around 1 kpc from the galaxy centre. The galaxy harbours a mildly active nucleus whose spectrum is dominated by emission lines characteristic of both LINER and HII regions. In total, 88 ring HII regions with $H\alpha$ fluxes larger than $10^{-18} \text{ erg/s/cm}^2$ were selected and characterised using their nebular spectra with the help of photoionisation and stellar population synthesis models (Cloudy and PopStar, respectively). These regions seem to be ionised by young clusters with mean ages of about 5 Ma. The chemical composition of the ionised gas was calculated using sulphur as a tracer and were found to be between 0.25 and 2.4 times the solar value, with most regions showing values slightly below solar. This result is consistent with an effective temperature of the cluster stars between 35000 K and 40000 K, as estimated from the ratio of HeI to H ionising photons. The high spatial resolution offered by MUSE allowed the measurement of the CNSFR sizes on the $H\alpha$ flux maps, all of which were spatially resolved. These measured sizes are fully consistent with those predicted by photoionisation models, thus leaving little room for photon escape and justifying the assumption of the regions being radiation bounded. The young ionising star clusters powering this radiation have masses of around $3.5 \times 10^4 M_{\odot}$, comparable to the mass of ionised gas and about 19 % of the corrected photometric cluster mass that includes a young non-ionising stellar population whose estimated age is around 300 Ma. A minor merger scenario is proposed for the formation of these clusters due to the counter rotating nature of the ring (Pizzella et al. 2004; de Zeeuw et al. 2002) and the homogeneity of abundances and continuum colours.

The present work is focused on three principal objectives: first, testing the capabilities of the new MEGARA instrument for the study of resolved kinematical components in the ionised gas of HII regions; second, determining the kinematic origin of such components if present, for which observing both recombination lines ($H\alpha$) and collisionally excited lines ($[NII]$ and $[SIII]$) is needed; and third, measuring the stellar velocity dispersion along the line of sight from the CaT lines in order to derive cluster dynamical masses. Accomplishing these objectives will ensure the cluster origin of the CaT lines and the reliability of this derivation. It should be said that a proper comparison between

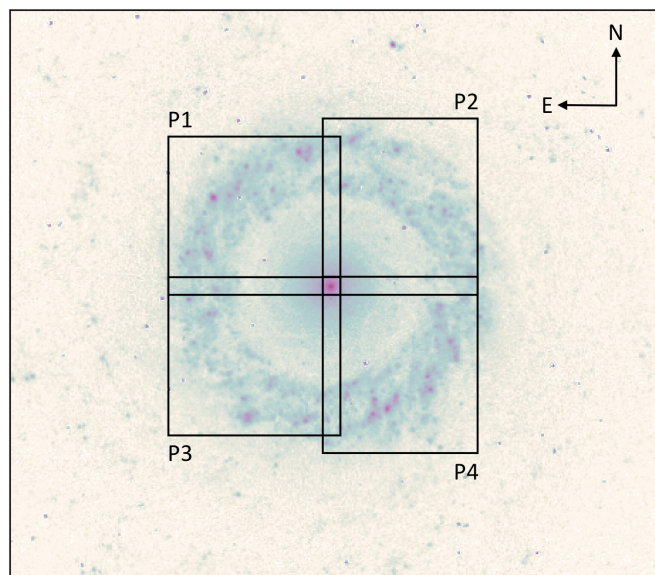


Fig. 1. WPC2-HST image in the F336W filter showing the circumnuclear region of NGC 7742 and the MEGARA fields of view. North is at the top and east is to the left.

ionising and dynamical masses for ionising young star clusters has not yet been done and is much needed.

In Sect. 2 we describe the observations and the reduction of the data, focusing on the new MEGARA observations. Section 3 is devoted to the presentation of our results. The discussion of cluster sizes and dynamical masses and the comparison between gas and star kinematical components is presented in Sect. 4. Finally, in Sect. 5 we summarise our work and present our conclusions.

2. Observations and data reduction

For this work we used data for the ring HII regions of NGC 7742 (J2000, RA=356.065542 deg, DEC=10.767083 deg, Skrutskie et al. 2006) obtained with the high-resolution integral field spectrograph MEGARA (Multi-Espectrógrafo en GTC de Alta Resolución para Astronomía, Carrasco et al. 2018) attached to the GTC 10.4 m telescope at La Palma Observatory. We used MEGARA in the integral-field Unit (IFU) mode working in the visible wavelength range from 3655 to 9700 \AA and providing a high spectral resolution (up to $R_{FWHM} = \lambda/\Delta\lambda \sim 20000$) and spatial resolution (0.62 arcsec spaxel size) simultaneously in a moderate size field of view (FoV) ($12.5 \times 11.3 \text{ arcsec}^2$). It has a total of 623 hexagonal fibres distributed in 567 science-fibres and 56 sky-fibres located at the edges of the FoV at distances from 1.7 arcmin to 2.5 arcmin from the centre of the fibre bundle.

The observations were acquired during three nights on 2021 August 28 and 31, and September 14¹ under spectroscopic conditions. The seeing during the observations ranged between approximately 0.7 and 0.9 arcsec and the airmass of the science images was always less than 1.25. Four pointings were needed to cover the whole circumnuclear ring extension of NGC 7742 (approximately the central $24 \times 24 \text{ arcsec}^2$; see Fig. 1).

Three dispersion elements (VPHs) were used: VPH863_HR (HR-I, $R_{FWHM} \sim 20500$), including the calcium triplet stel-

¹ Proposal GTC28-21A: *A high spatial and spectral resolution study of circumnuclear star-forming regions*
PI: Ángeles I. Díaz. Semester 2021-A.

Table 1. Target observations.

Target	RA (hh:mm:ss.ss)	DEC (dd:mm:ss.ss)	Field of View Position Angle ^a (degrees)	Exp. Time ^b (s)		
				VPH863_HR	VPH890_LR	VPH665_HR
NGC7742_P1	23:44:16.02	10:46:05.80	0	1050	450	684
NGC7742_P2	23:44:15.28	10:46:06.40	0	1050	-	684
NGC7742_P2	23:44:15.28	10:46:06.40	90	1050	450	342
NGC7742_P3	23:44:16.02	10:45:55.60	0	1050	450	684
NGC7742_P4	23:44:15.28	10:45:55.00	90	1050	450	342

Notes. ^a From north towards east. The orientation of 0 deg implies that the north is aligned with the short side and the east–west axis with the long side of the detector. ^b Total target observed time without overheads.

Table 2. Extraction parameters for emission line and continuum maps.

MEGARA				
Line	λ_c (Å)	$\Delta\lambda$ (Å)	$\Delta\lambda_{left}$ (Å)	$\Delta\lambda_{right}$ (Å)
H α	6563	5	6596 - 6606	6530 - 6540
[SIII]	9532	10	9472 - 9492	9545 - 9565
Continuum	8810	5	-	-
MUSE				
Line	λ_c (Å)	$\Delta\lambda$ (Å)	$\Delta\lambda_{left}$ (Å)	$\Delta\lambda_{right}$ (Å)
H α	6563	8	6531.5 - 6539.5	6597 - 6605
[SIII]	9069	15	9010 - 9040	9115 - 9145
Continuum	8810	5	-	-

Notes. All wavelengths are in the rest frame.

lar lines (CaT) at high spectral resolution; VPH890_LR (LR-Z, $R_{FWHM} \sim 5800$), including the [SIII] $\lambda\lambda 9069, 9532$ Å emission lines and the CaT lines at low resolution; and VPH665_HR (HR-R, $R_{FWHM} \sim 20050$), including the [NII] $\lambda\lambda 6548, 84$ Å, H α , and [SII] $\lambda\lambda 6717, 32$ Å emission lines at high resolution. A relation of the total integration times and their splitting in different exposures for each of the used set-ups is given in Table 1. Using these configurations, velocity dispersions of around 6.4 km/s and 22.5 km/s in full width at half maximum (FWHM) were expected at high and low spectral resolutions, respectively.

Calibration images were acquired on the observing nights and on the preceding and following nights. They consisted of bias frames to create a CCD spatial response function; flat-field frames necessary for locating each fibre spectrum on the CCD and for performing a spatial instrumental response function; arc calibration exposures needed for wavelength calibration; and three spectrophotometric standard star exposures needed for performing a spectral instrumental response function. The standard procedures of bias subtraction, tracing and extraction of each fibre spectra, flat-field correction, and wavelength calibration were followed applying some required modifications to the standard MEGARA pipeline (Pascual et al. 2018)² using the calibration files present in Cardiel & Pascual (2018). Flux calibration was not needed for our work, and we decided not to do it in order not to introduce additional errors in our subsequent analysis. After the reduction procedure, one data cube per pointing was produced (i.e. eight, five, and four cubes for the HR-R, HR-I, and LR-Z set-ups, respectively) with a spatial binning of 0.2 arcsec/pix.

Astrometric alignment was achieved by comparing our MEGARA data with those extracted from the publicly available observations of NGC 7742 obtained by the IFS MUSE

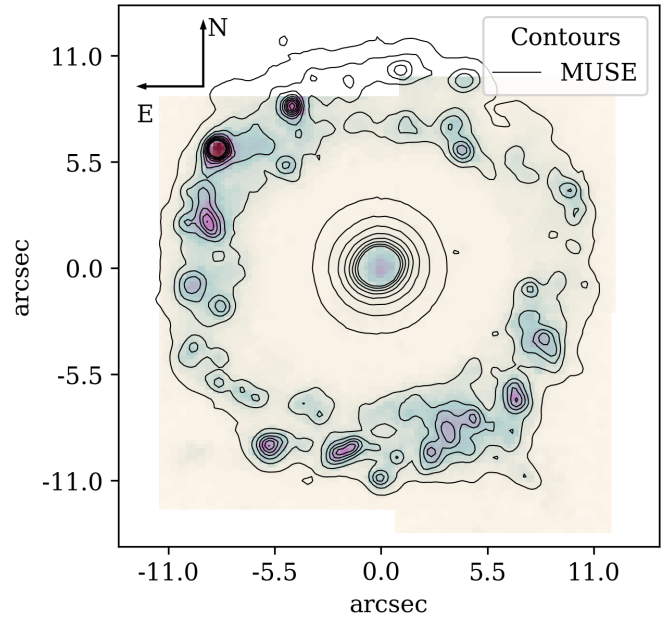


Fig. 2. Example of HR-R final data cube compressed in the spectral direction. Superimposed are the contours of the MUSE data (same range of wavelengths). The colour scale is linear. North is up and east to the left.

(Science Verification run on 2014 June 22, ESO Programme 60.A-9301(A), M. Sarzi) and already analysed in Zamora & Díaz (2023b). The 2D cross-correlation technique proposed by Tonry & Davis (1979) was used to find the spatial shift between MEGARA and MUSE data. We constructed H α and [SIII] $\lambda 9532$ Å emission line maps for the HR-R and LR-Z set-ups, respectively, and a continuum map near the CaT absorption lines for the HR-I set-up. For the emission line maps, a linear behaviour of the continuum emission in the region of interest was assumed choosing appropriate side-bands of a given width for each line. Table 2 lists in Cols. 1 to 5 (from left to right): the identification of each line; its central wavelength; its width; and the limits of the two continuum side-bands. The upper and lower table panels show these parameters for the MEGARA and MUSE data, respectively. The followed procedure ensures that our pointings are correctly aligned.

Finally, we combined the overlapping individual cubes into a single cube using the average of the data available in each pixel with no spatial smoothing applied. Figure 2 shows the resulting cube for HR-R set-up as an example. It is compressed in the spectral direction, and the contours of the data obtained with MUSE

² see <https://github.com/guaix-ucm/megaradrp/>

showing the consistency with those obtained from MEGARA are superimposed.

3. Results

3.1. HII region selection

The HII region selection was accomplished as described in the first paper of this series (see Zamora & Díaz 2023b) consisting in the application of an iterative procedure for the detection of high-intensity clumps on an $H\alpha$ emission line map. This method requires as input the maximum and minimum extent of regions (500 pc and the point spread function of observations, respectively) and the relative flux intensity in each of the regions with respect to the emission of its centre (10%). Then, the program tried different values for the absolute flux intensity background of the complete map adopting the one that minimises the dispersion of the spatial residuals in the map.

We consider that this HII region segmentation is appropriate for our MEGARA study since the astrometry correction was made with respect to MUSE data. In addition, since the selected pixel scale for the cube construction is the same as the MUSE scale (0.2 arcsec/pix) we can assure that all the ring HII regions are spatially resolved. Additionally, the measured angular radii of the regions calculated using this method were found to be compatible with radiation bounded ionised nebulae (see Zamora & Díaz 2023b). Regions R2, R13, R24, R39, R40, R46, R49, R68, and R82 fall outside the area covered by the FoV of MEGARA, and therefore are not included in the present study. In the end, we selected a total of 79 HII regions in the ring.

3.2. Nebular emission line measurements

We extracted each region spectrum by integrating the flux inside its corresponding aperture and we used the code LiMe (LiNE MEasuring library Fernández et al. 2022) to separate the different kinematical components present in each emission line. This program uses a defined window for each line and two additional ones to calculate the continuum below. After the fitting, we took into account only those components that meet the requirement $A_g > 3\sigma_l$, with A_g being the Gaussian amplitude and σ_l the local standard deviation of the continuum bands selected for each fit. Next, we measured the radial velocity, v , and the velocity dispersion, σ , of each component in the following emission lines: $H\alpha$, [NII] $\lambda\lambda 6548,84$ Å and [SII] $\lambda\lambda 6716,31$ Å from the HR-R set-up, and [SIII] $\lambda\lambda 9069,9532$ Å from the LR-Z set-up. We performed an individual fitting for each emission line and adopted a kinematical bond between the components of lines of the same element: [NII] $\lambda 6548$ Å with [NII] $\lambda 6584$ Å; [SII] $\lambda 6716$ Å with [SII] $\lambda 6731$ Å; and [SIII] $\lambda 9069$ Å with [SIII] $\lambda 9532$ Å.

Figure 3 shows two examples of the procedure for regions R1 and R9; the panels show (from left to right) the following emission lines: $H\alpha$ and [NII] $\lambda\lambda 6548,84$ Å; [SII] $\lambda\lambda 6716,31$ Å; and [SIII] $\lambda 9069$ Å and [SIII] $\lambda 9532$ Å. Eight regions out of 79 (~ 10%), labelled R6, R48, R78, R79, R81, R84, R85, and R88, were found to have one only component; the rest show at least two components in the $H\alpha$ emission line; and only one region, R1, shows two components in the [SIII] lines. In this region, which is shown in the top panel of the figure, three components are clearly identified in the $H\alpha$ and [NII] lines, and also a second can be seen in the [SIII] $\lambda 9532$ Å emission line. The region is located near a supernova event: SN 1993R.

The measured velocities were corrected to rest frame using the redshift derived value of $v = 1652.364$ km/s ($z = 0.00553$).

Errors in the velocity of each component are given by the LiMe code using a Monte Carlo procedure and the noise calculated in the continuum bands. Table 3³ shows the velocity results in columns 1 to 6: (1) the region ID; (2) the line component; and (3-6) the velocity of the $H\alpha$, [NII], [SII], and [SIII] emission lines, respectively. The corresponding errors in the velocity dispersions were calculated as the difference between the FWHM of the largest and smallest fitted Gaussian function taking into account the noise of the fitted spectrum. Using the amplitude of the fitted Gaussian, A_g , and the noise calculated in the residuals of the fit, σ_f , the error can be calculated as

$$\Delta[\sigma] = \frac{\sigma}{2\sqrt{\ln(2)}} \cdot \ln\left(\frac{1 + \sigma_f/A_g}{1 - \sigma_f/A_g}\right). \quad (1)$$

The measured velocity dispersions of the gas needs to be corrected for instrumental dispersion, σ_{inst} and thermal broadening, σ_{th} , and hence the corrected value for the gas velocity dispersion is

$$\sigma_{gas} = \sqrt{\sigma_{measured}^2 - \sigma_{inst}^2 - \sigma_{th}^2}. \quad (2)$$

The instrumental dispersion values are 6.4 km/s and 22.5 km/s for the MEGARA high- and low-resolution configurations, respectively (see Sect. 2). The thermal broadening can be calculated assuming a Maxwellian velocity distribution of the ions using the equation

$$\sigma_{th} = \sqrt{\frac{k \cdot t_e}{m}}, \quad (3)$$

where k is the Boltzmann constant ($k=1.380649 \times 10^{-23}$ J/K), t_e is the electron temperature in degrees Kelvin, and m is the mass of the ion involved ($m_{H^+} = 1.6726 \times 10^{-27}$ kg; $m_{N^+} = 2.3257 \times 10^{-26}$ kg; $m_{S^+} = 5.3244 \times 10^{-26}$ kg; $m_{S^{++}} = 5.3243 \times 10^{-26}$ kg). We assumed the electron temperature of [SIII] (t_e [SIII]) calculated in Zamora & Díaz (2023b) for each CNSFR; its average value is 7967 K, and hence the mean thermal corrections are 8.11 km/s for H^+ ; 2.17 km/s for N^+ ; and 1.44 km/s for S^+ and S^{++} .

Tables 3 and 4 show the velocity and velocity dispersion results in columns 1 to 6: (1) the region ID; (2) the line component; (3-6) the velocity or velocity dispersion of the $H\alpha$, [NII], [SII], and [SIII] emission lines, respectively.

3.3. Stellar absorption lines

The main objective of our work is to estimate the properties of the stellar population of the clusters associated with the observed CNSFRs. In order to do this, we used two sets of absorption lines: the MgIb triplet at 5167-5183 detected in the MUSE data (unresolved) and the CaII triplet (CaT) at $\lambda\lambda$ 8498, 8542, 8662 Å (CaT) resolved with MEGARA.

We measured the equivalent widths (EWs) of these stellar absorption lines by integrating the line fluxes and taking as continuum values the linear interpolation between the mean integrated fluxes in 30 Å continuum bands on both sides of the line. The details of the measuring procedure can be seen in Table 8 in Zamora & Díaz (2023a). The EW errors were calculated using the standard deviation in the two continuum bands and propagating them

³ The accuracy of the fit and the number of components have been determined by analysing the chi-square of the residuals.

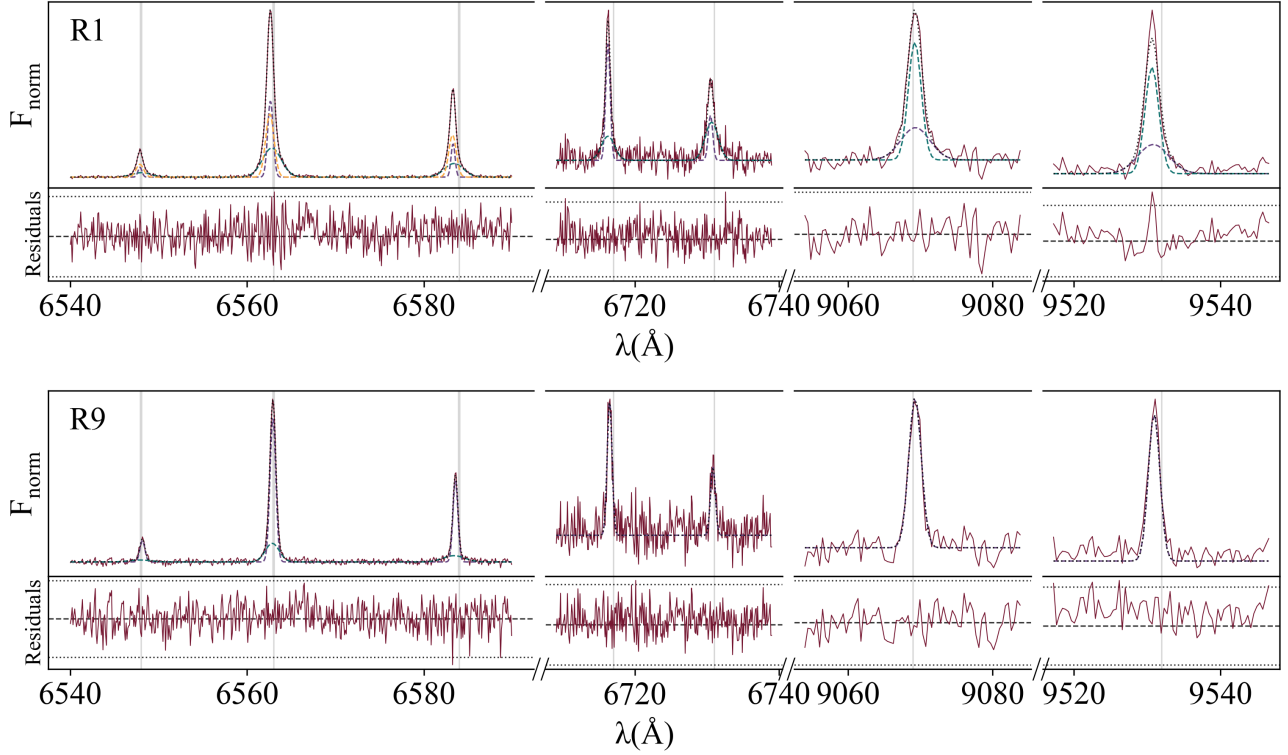


Fig. 3. Spectra of regions R1 and R9 (top and bottom panels, respectively) showing the kinematical components fitted. From left to right: $H\alpha$ and $[\text{NII}]\lambda\lambda 6548, 6584 \text{ \AA}$; $[\text{SII}]\lambda\lambda 6717, 6731 \text{ \AA}$; $[\text{SIII}]\lambda 9069 \text{ \AA}$; and $[\text{SIII}]\lambda 9532 \text{ \AA}$ emission lines.

Table 3. Emission line radial velocities in km/s.

Region ID	Component	$v(H\alpha)$ (km/s)	$v([\text{NII}]\lambda 6584 \text{ \AA})$ (km/s)	$v([\text{SII}]\lambda 6717 \text{ \AA})$ (km/s)	$v([\text{SIII}]\lambda 9532 \text{ \AA})$ (km/s)
R1	Narrow	8.45 ± 0.41	8.36 ± 8.52	6.80 ± 0.65	6.71 ± 1.71
	Broad	5.48 ± 0.85	5.76 ± 12.02	7.00 ± 5.35	12.20 ± 9.46
	Additional	15.4 ± 1.2	12.86 ± 37.74	-	-
R3	Narrow	16.76 ± 0.09	16.57 ± 2.90	16.23 ± 0.58	15.42 ± 0.93
	Broad	20.70 ± 0.95	18.72 ± 25.72	31.55 ± 9.52	-
R4	Narrow	31.52 ± 0.20	32.54 ± 2.70	30.17 ± 1.12	30.07 ± 1.29
	Broad	36.34 ± 0.78	36.35 ± 19.61	44.89 ± 5.20	-
	Additional	18.2 ± 6.8	-	-	-

Notes. The complete table is available online; only a part is shown here as an example.

Table 4. Emission line velocity dispersions in km/s.

Region ID	Component	$\sigma(H\alpha)$ (km/s)	$\sigma([\text{NII}]\lambda 6584 \text{ \AA})$ (km/s)	$\sigma([\text{SII}]\lambda 6717 \text{ \AA})$ (km/s)	$\sigma([\text{SIII}]\lambda 9532 \text{ \AA})$ (km/s)
R1	Narrow	10.29 ± 0.09	7.88 ± 0.15	12.41 ± 0.80	18.98 ± 0.53
	Broad	19.60 ± 0.20	18.30 ± 0.28	40.22 ± 4.14	62.64 ± 6.50
	Additional	47.7 ± 1.1	48.30 ± 2.34	-	-
R3	Narrow	14.46 ± 0.08	12.67 ± 0.13	13.82 ± 0.65	13.68 ± 0.44
	Broad	43.68 ± 1.66	34.51 ± 2.02	53.56 ± 8.84	-
R4	Narrow	10.53 ± 0.12	12.44 ± 0.21	12.00 ± 1.34	14.06 ± 0.58
	Broad	27.88 ± 0.59	45.04 ± 3.09	33.12 ± 3.54	-
	Additional	69.2 ± 10.3	-	-	-

Notes. The complete table is available online; only a part is shown here as an example.

Table 5. Equivalent widths of stellar absorption lines of the observed CNSFRs.

Region ID	EW(CaII) ^a (Å)	EW(MgI) (Å)
R1	7.307 ± 0.264	1.686 ± 0.035
R3	7.301 ± 0.278	2.329 ± 0.063
R4	7.558 ± 0.303	1.868 ± 0.044
R5	7.418 ± 0.338	2.147 ± 0.048
R6	7.118 ± 0.318	2.141 ± 0.073
R7	6.732 ± 0.339	1.972 ± 0.056
R8	7.350 ± 0.299	2.156 ± 0.060
R9	7.571 ± 0.346	2.013 ± 0.054
R10	7.008 ± 0.297	1.987 ± 0.048
R11	7.281 ± 0.211	2.840 ± 0.092

Notes. ^a($\lambda 8542\text{\AA} + \lambda 8662\text{\AA} + \lambda 8498\text{\AA}$). The complete table is available online; only a part is shown here as an example.

in quadrature. In principle, absorption line EW measurements in objects with different velocity dispersions should be for the broadening of the spectral lines; this effect decreases the continuum level providing lower EW values. However, this correction for MUSE data was found to be negligible ($< 1\text{\AA}$ for velocity dispersions of around 170 km/s for MUSE spectral resolution), and so no correction was applied. Table 5 lists in columns 1 to 3: (1) the region ID; (2) the CaT EW in Å; and (3) the MgIb EW also in Å.

The presence of a non-negligible contribution by the nebular continuum can dilute the starlight weakening and distorting the absorption features. This component is usually not taken into account, but it provides information about the origin of the features measured. Thus, we calculated a dilution factor, D , for each set of lines with respect to a reference average value measured in the spectra of normal spiral galaxy nuclei, which corresponds to old metal-rich stellar populations ($EW_{ref}(\text{CaII}) = 7.7 \pm 0.5\text{\AA}$, $EW_{ref}(\text{MgI}) = 5.18 \pm 0.71\text{\AA}$; Terlevich et al. 1990; Keel 1983). We calculated this dilution factor as the ratio of the measured EWs to the adopted reference values, $D = EW_{obs} / EW_{ref}$, and compared it to the dilution produced by the nebular continuum associated with a nebula ionised by a young star cluster synthesised using the PopStar code (Mollá et al. 2009) with Salpeter’s IMF ($m_{low} = 0.85 M_{\odot}$, $m_{up} = 120 M_{\odot}$ Salpeter 1955) and an age of 5.5 Ma.

Figure 4 shows the comparison between the dilution factors, D , calculated for the MgIb and CaT stellar absorption features for the studied CNSFRs. The red lines represent the dilution produced by the nebular continuum in the optical and near-IR. We can see that the mean value of the MgIb dilution is about 50%, consistent with the contribution by a nebular continuum. However, the CaT lines are shown almost undiluted. This result can be explained by the presence of red supergiant stars whose CaT features are stronger than those in normal early spiral galaxies, while the reference value probably consists of a stellar population dominated by red giants. This points to the occurrence of a relatively recent star formation episode. The same behaviour has already been found for circumnuclear star clusters in both rings of NGC 7469 (see Zamora & Díaz 2023a) and in earlier work (Terlevich et al. 1990; García Vargas et al. 1993; Oliva et al. 1995).

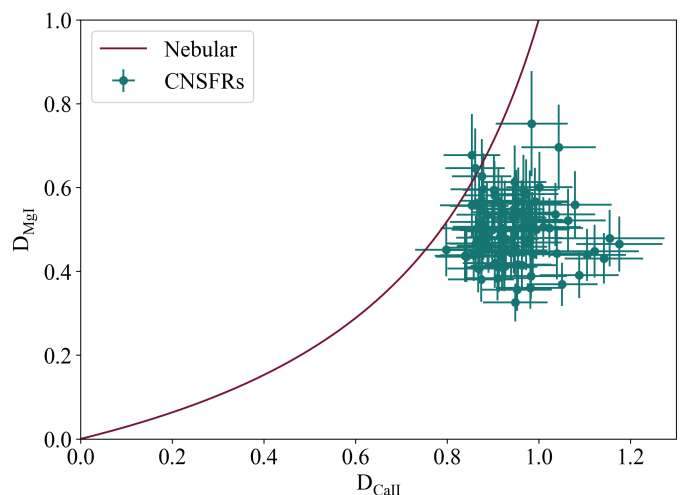


Fig. 4. Comparison between the dilution factors calculated for the MgIb and CaT stellar absorption features for the observed CNSFRs. The red lines represent the dilution produced by the nebular continuum in the optical and near-IR.

3.4. Stellar velocity dispersions

Stellar velocity dispersions can be obtained from the stellar absorption lines. In the second paper of this series (see Zamora & Díaz 2023a) we used the CaT lines detected in the MUSE data for this calculation. However, the spectral resolution reached in the MUSE data was insufficient to resolve the CaT lines in the case of the HII ring regions in NGC 7742, and therefore we acquired higher resolution data using MEGARA, which provides about 14 km/s of spectral resolution (see Sect. 2). As in the case of NGC 7469, the clusters studied in this work have red supergiant stars dominating the near-IR range of the spectrum and the CaT $\lambda\lambda$ 8498, 8542, 8662 Å lines (see Sect. 3.3) are easily detected. The use of the near-IR spectra provides two principal advantages for this study: there is little contamination by TiO bands and nebular lines, and the velocity resolution at longer wavelengths is higher than in the blue part of the spectrum for the same spectral dispersion. Additionally, using the cross-correlation technique, stellar weak lines present in this part of the spectra also contribute to the goodness of the results.

We used the cross-correlation technique proposed by Tonry & Davis (1979). In this traditional method, a comparison between a stellar template with the observed stellar population spectrum is done. The assumption made assumes that a galaxy spectrum can be represented by the sum of different stellar spectra with different velocity offsets convolved with a broadening function: $g \sim \alpha[t(n) * b(\lambda - \delta)]$, where b is the broadening function; g and t are the cluster and the stellar template spectra, respectively; and δ is the velocity shift between the stars. The width of this broadening function is calculated using two correlations: the cluster spectrum with the stellar template ($g \otimes t$) and the stellar template with itself ($t \otimes t$). The convolution products are applied assuming a periodic spectrum with discrete Fourier transforms, and the broadening function is assumed to be Gaussian. However, this last assumption is not correct for the ($t \otimes t$) correlation at spectral resolutions as high as the one provided by MEGARA, and this technique needs to be modified. We used the adapted methods proposed in Zamora & Díaz (2023c) of the ($g \otimes g$) correlation, which is broader than the other two and whose Gaussian behaviour can be ensured. In order to test these two additional methods and the traditional ones with our data, we

selected a region with high S/N (R52, located in the pointing with the higher exposure time in the HR-I set-up). For the stellar template, we used late-type red giants and supergiants obtained from the MEGARA stellar library (García-Vargas et al. 2020) aligning all available stellar spectra in velocity and calculating the average between them, verifying that no apparent broadening is introduced in the procedure. The use of only two stellar types of stars for the correlation analysis could introduce errors in our velocity dispersion measures. However, the use of CaT lines minimises the mismatch between the stellar template and the cluster spectrum since they are very strong in most stars of moderate to high metallicity.

The top panel of Fig. 5 shows the stellar spectrum of the selected cluster R52 at high and low MEGARA spectral resolutions, with red and purple lines respectively. The stellar template is shown with a blue line and the nebular lines present in this spectral range are marked. We can see that the S/N values of these spectra are low, even in this region that was observed with twice the average exposure time. This could be due to the noise component or to errors associated with the subtraction of the sky background, which is very prominent in the near-IR. Thus, we calculated a mean spectrum of the sky, using the MEGARA fibres earmarked for this purpose. The lower panel of the figure shows this spectrum, which shares some features with the cluster spectrum.

We used the modified version of the Tonry & Davis method described above for the application of the cross-correlation technique to the data obtained from the MEGARA in the HR-I configuration in the spectral range 8450 Å to 8850 Å. Prior to this, we binned the spectrum into 4069 logarithmic wavelength bins corresponding to a velocity resolution of ~ 3.4 km/s. Then, we estimated the continuum by fitting a second-order polynomial after masking the features present in the spectrum. The masks were built assuming a width of 3 Å and 10 Å on each side of the central wavelength of the nebular and stellar lines involved, respectively. This continuum was subsequently subtracted.

Next, the high- and low-frequency variations were filtered using a band-pass filter in the Fourier spectrum transform. The minimum and maximum wave numbers are $k_{min} = 3$ and $k_{max} = 350$, which correspond to wavelength values lower than 10 Å and to the nominal MEGARA/HR-I spectral resolution. The low-frequency variations are associated with continuum subtracted errors and the high-frequency variations with the noise component. Figure 6 shows, in a small range of wavelengths, in light red the original spectrum and in dark red the spectrum after the band-pass filter. The stellar template is also shown in blue for comparison. We can see that this filter removes part of the noise, recovering some stellar features. However, the S/N continues to be low and we can see residuals, for example in the central part of the strongest line. Thus, the noise present in our spectrum probably comes from the errors associated with the pipeline sky subtraction. Therefore, we decided to use the data without the sky subtraction to be able to quantify this additional component in the cross-correlation technique and to obtain a more reliable result in the stellar dispersion determination.

An important step in the cross-correlation procedure is the subtraction of the non-stellar component of the spectra, which can introduce errors in the velocity dispersions of up to 5 km/s (see Zamora & Díaz 2023c). In order to remove correctly the nebular component of the spectrum, we first removed the proper motion of the cluster by shifting the spectrum to the rest-frame position. For this step, we used the position of the $(g \otimes t)$ cross-correlation.

Then, we masked the nebular lines shown in Fig. 5 assuming a width of 0.4 Å at each side of their central wavelength.

Finally, we calculated four cross-correlation functions for this HII region, $(t \otimes t)$, $(g \otimes t)$, $(g \otimes g)$, and $(s \otimes s)$, with t being the stellar template, g the cluster spectrum, and s the mean sky spectrum of our observations. The top panel of Fig. 7 shows the $(s \otimes s)$ correlation. Two components can be seen, one associated with the sky lines and another associated with the detector response. They were fitted with two Gaussian functions and their widths are $\mu_{ss1} = 0.2098$ Å and $\mu_{ss2} = 12.1445$ Å, respectively. The width of the first component corresponds to a value of $\Delta\lambda = 0.15$ Å in σ -units, which is slightly lower than the MEGARA resolution for this set-up, $\Delta\lambda = 0.18$.

The top panel of Fig. 7 shows, as an example, the $(g \otimes g)$ correlation for the R52 cluster. In this figure we can identify the component associated with the sky lines and the component associated with the stars of the cluster. According to this, we fitted simultaneously two Gaussian functions, one of them using the μ_{ss1} value calculated for the $(s \otimes s)$ correlation. The width of the cluster component is $\mu_{gg} = 2.2680$ Å. The correlation $(g \otimes t)$ is shown in the lower panel of the same figure. In this case the sky emission affects only the cluster spectrum, and hence the sky component does not show up. The cluster component is $\mu_{gt} = 2.1147$ Å.

We combined these results, together with the width of the $(t \otimes t)$ correlation function ($\mu_{tt} = 1.241$ Å) and we applied the three methods studied in Zamora & Díaz (2023c):

$$(i) \quad \sigma = \sqrt{\frac{\mu_{gg}^2 - \mu_{tt}^2}{2}},$$

$$(ii) \quad \sigma = \sqrt{\mu_{gg}^2 - \mu_{gt}^2},$$

$$(iii) \quad \sigma = \sqrt{\mu_{gt}^2 - \mu_{tt}^2}.$$

The last equation is the one proposed by Tonry & Davis (1979). We performed these calculations for R52, correcting methods (i) and (ii) for the non-Gaussian behaviour of the $(t \otimes t)$ correlation. The final results are (i) $\sigma = 27.87$ km/s; (ii) $\sigma = 28.42$ km/s; and (iii) $\sigma = 28.44$ km/s. We can see that the three methods show very similar results, and thus we can conclude that the reduction and treatment of these high-resolution data and the application of the cross-correlation method is correct.

Therefore, for the rest of the CNSFRs, we decided to apply method (iii) in order not to use the $(g \otimes g)$ correlation, due to the sky subtraction problems. The velocity dispersion errors were calculated as the semi-difference between the largest and smallest Gaussian width that can be fitted considering the asymmetries in the correlation peak, as suggested in Zamora & Díaz (2023c), although it could lead to the error being somewhat overestimated. Applying the described methodology, we obtained reliable CaT velocity dispersion values for 30 of the selected CNSFR regions. They are shown in Table 6, and they take values from 14.3 to 77.1 km/s.

4. Discussion

4.1. Cluster sizes

We calculated the effective radii of the star clusters from the *Hubble* Space Telescope (HST) continuum image. These data were acquired on 2009 November 5 with the Wide Field and Planetary

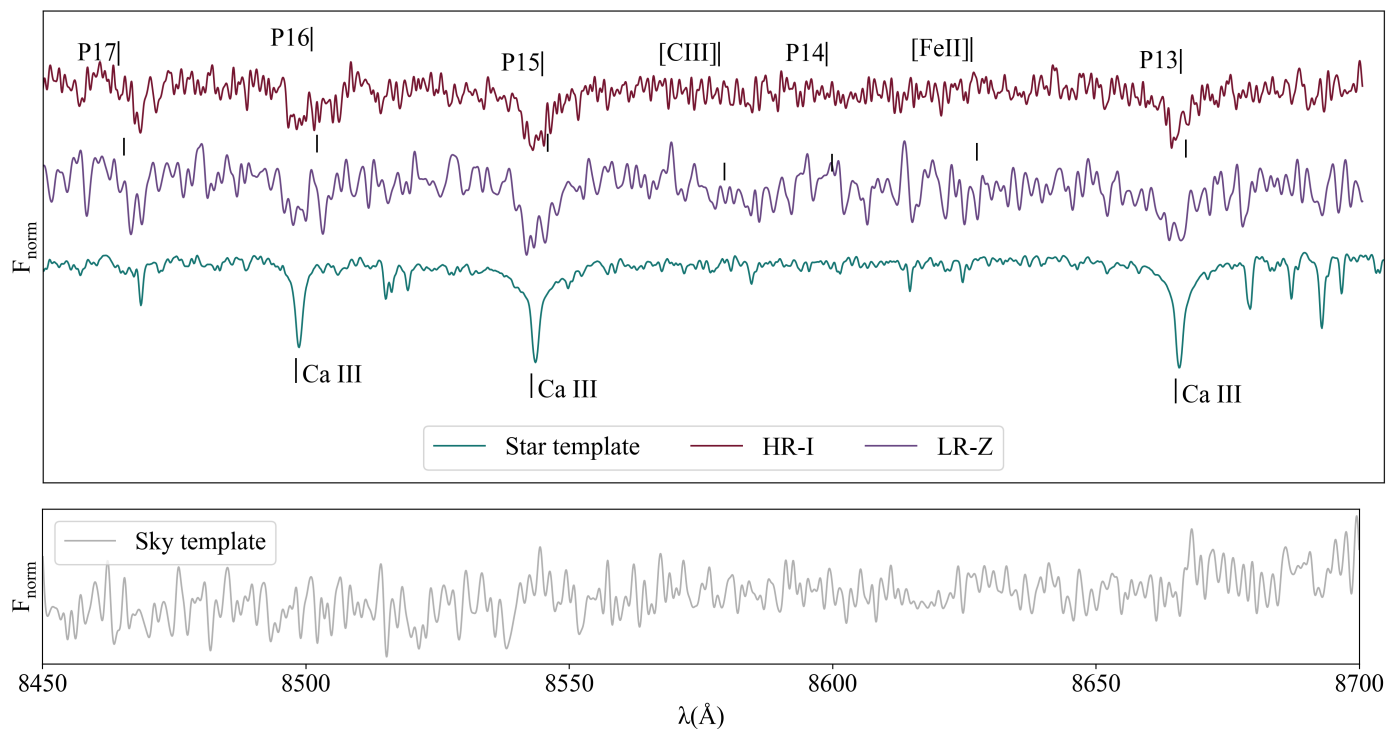


Fig. 5. Typical spectra used to measure the stellar velocity dispersions. Top panel: R52 absorption spectrum from MEGARA/HR-I and LR-Z configurations shown as red and purple lines, respectively. The absorption stellar lines and emission lines present in this wavelength range are indicated. The stellar template is also shown as a blue line. Bottom panel: Sky template (see text).

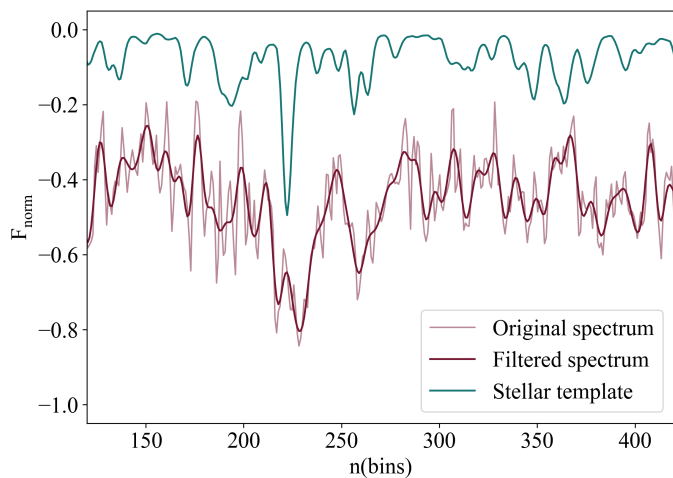


Fig. 6. Absorption line spectrum of R52 from the MEGARA/HR-I configuration, in logarithmic wavelength. The light and dark red lines show the spectrum before and after applying the pass-band filter for higher frequencies. The stellar template is also shown (blue line).

Camera 2 (WFPC2) and the F555W continuum filter where stellar clusters are easily identified. These data are a part of proposal 6276 (IP: J. Westphal) organised in three exposures of 480 s. The data were downloaded from the *Hubble* Legacy Archive and reduced by the Space Telescope Science Institute (STScI) using the available calibration files taken for this observation and keeping in mind different dithering positions.

The effective radii of the star clusters were calculated using the following procedure. First, we estimated the region background by fitting a three-order polynomial. After subtracting it, we fitted the surface brightness of each knot present in the ob-

served clusters assuming a two-dimensional Gaussian profile. Figure 8 shows two examples of the described procedure as applied to regions R1, and R52. The left panels of the figure show the F555W WFPC2-HST image for each selected region and the right panels show the same image after background subtraction. Selected clusters are shown by blue circles. The radius of each knot is taken as $1/2 \cdot \text{FWHM}$. There are three regions, R72, R75, and R88, where no knot is readily appreciable in the continuum at 5550 Å, and thus we did not calculate their sizes.

As opposed to other CNSFRs from the literature, this galaxy does not seem to have large star-forming complexes, and $\sim 60\%$ of the CNSFRs (16 out of 27) seem to host single clusters and $\sim 27\%$ (7 out of 27) are composed of two clusters. Three regions show three different knots, and one shows four. We can compare these values with the results obtained for NGC 7469 (see Zamora & Díaz 2023a), which shows two regions with respectively 20 and 19 knots, and only 15% (4 of 27) seem to have only one star cluster. These last results, are similar to those found for the regions analysed in NGC 2903 showing more than 20 knots (Hägele et al. 2009), NGC 3310 hosting two great complexes with 28 and 30 clusters each (Hägele et al. 2010), and NGC 3351 with a large region showing 17 distinct knots (Hägele et al. 2007). In the case of NGC 7469, we imagine this effect to be due to the galaxy being further away since in this case we may be selecting larger star-forming complexes, due to lack of spatial resolution; however, the distances to the other three galaxies mentioned are of the same order as the one studied here. In particular, NGC 3310 at a similar distance to NGC 7742 seems to have only one region hosting an individual knot. It is probable that the difference between the CNSFRs is related to their different formation processes which in the latter case seem to be due to gas accretion after a minor merger event.

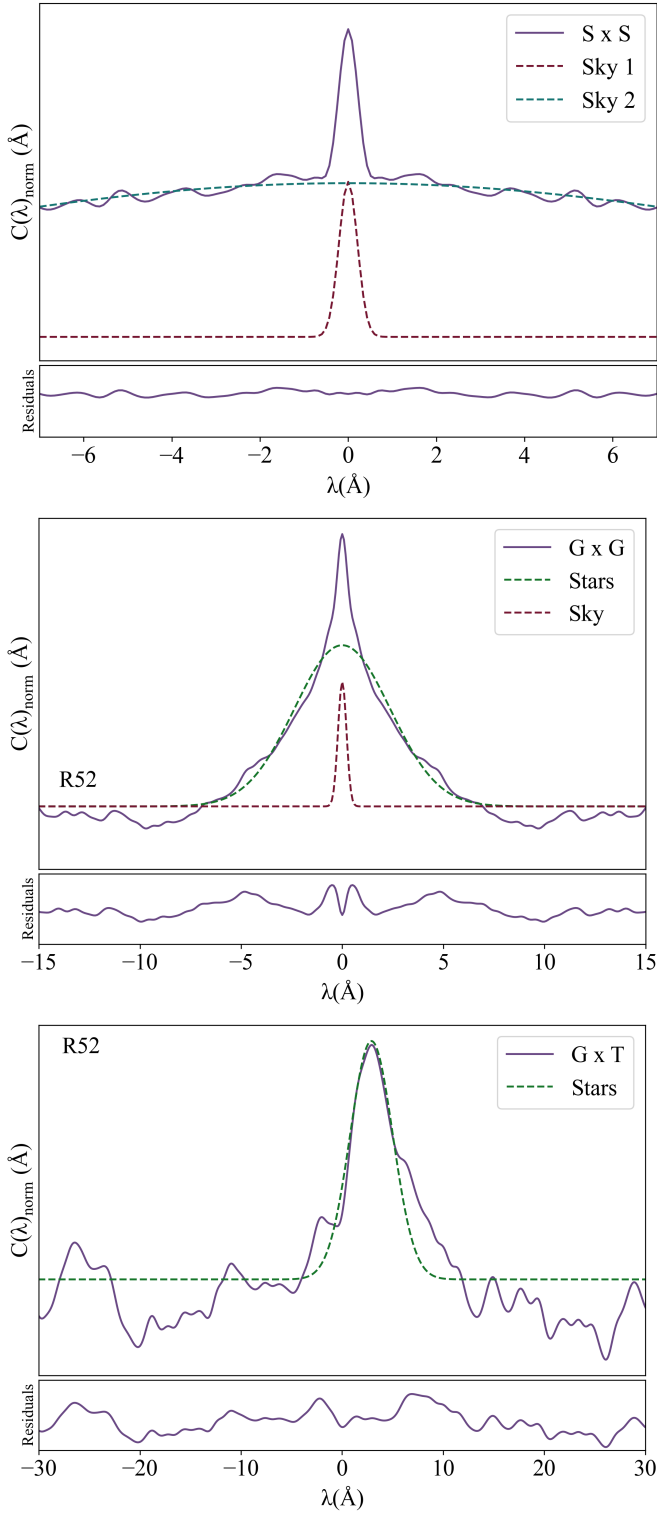


Fig. 7. Example of auto-cross-correlations calculated in this work. Top panel: Auto-cross-correlation function of the sky template. Middle panel: Auto-cross-correlation of the spectrum of region R52. Bottom panel: Cross-correlation between the cluster spectrum and the stellar template. The lower panel of each plot shows the residuals of the fitting.

The effective radii of the studied single knots range between 8.5 and 60.5 pc, with a mean value of 12.6 pc. Figure 9 shows the distribution of the radius of each knot for the CNSFRs in this work and those found in the literature used for comparison (Hägele et al. 2009, 2007, 2010). The range of radius found for

Table 6. Stellar cluster velocity dispersions in units of km/s.

Region ID	$\sigma_*(\text{CaT})$ (km/s)
R1	22.61 ± 6.65
R3	31.43 ± 4.68
R5	77.08 ± 1.37
R7	20.19 ± 4.39
R8	37.75 ± 19.32
R14	19.34 ± 5.87
R15	27.88 ± 6.61
R16	50.82 ± 3.95
R22	37.10 ± 9.98
R23	38.75 ± 8.66
R26	19.26 ± 6.86
R31	45.87 ± 9.38
R33	47.73 ± 5.41
R36	72.04 ± 0.49
R41	50.82 ± 4.95
R45	56.26 ± 14.67
R47	38.95 ± 13.01
R50	44.64 ± 4.94
R51	36.78 ± 6.83
R52	28.40 ± 9.85
R53	50.53 ± 1.13
R55	44.67 ± 7.63
R57	14.46 ± 4.49
R60	33.36 ± 7.53
R63	32.93 ± 7.31
R69	14.25 ± 6.79
R72	26.40 ± 4.24
R74	23.56 ± 5.80
R75	43.76 ± 6.35
R88	20.65 ± 3.52

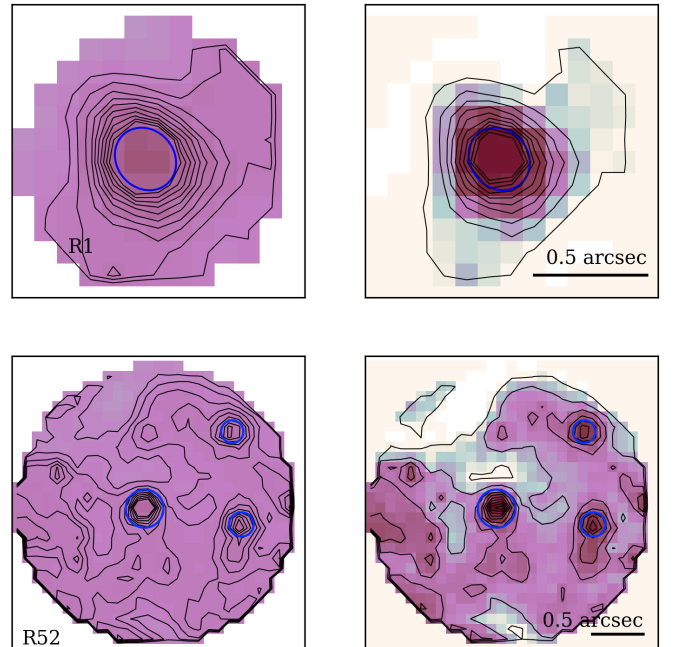


Fig. 8. Results of the stellar cluster radius measurement procedure for regions R1 and R52, upper and lower panels, respectively (see text for details). The angular scale is given in the corner of each panel.

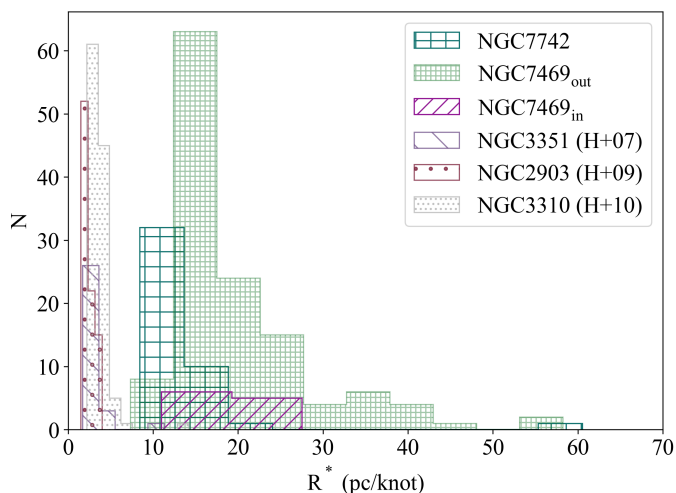


Fig. 9. Histograms of the distributions of the radius of each knot in the CNSFRs of NGC 7742 compared to those using data from the literature.

NGC 7469 is wider than in the other galaxies, and the same is true for the mean radii for the inner and outer ring regions. On the other hand, NGC 3351, NGC 2903, and NGC 3310 have smaller knots than NGC 7742.

4.2. Dynamical masses

We calculated the dynamical masses for each observed cluster from its measured CaT velocity dispersion and size assuming a virialised system and using the expression given by (Ho & Filippenko 1996a,b)

$$M^{dyn} = 3 \cdot \sigma^2 \cdot \frac{R}{G}, \quad (4)$$

where σ is the one-dimensional velocity dispersion of the system, R is its radius, and G is the gravitational constant.

This calculation assumes that the clusters (i) have spherical symmetry; (ii) are gravitationally bound; and (iii) have an isotropic velocity distribution. Most of the clusters show only one knot, and thus the calculated masses under this assumption seem to be appropriate. However, a small number are clearly multiple; in this case the total mass of the cluster was estimated by adding the masses of its individual knots inferred using the velocity dispersion of the entire region a procedure that most likely result in an overestimate.

Figure 10 shows the distribution of the cluster dynamical masses for NGC 7742 compared with those of the inner and outer rings of NGC 7469. We can see that NGC 7742 knots show lower masses, which is to be expected from their smaller sizes. However, they tend to be more massive than the CNSFRs from the literature (Hägele et al. 2010, 2007, 2009, NGC 3351, NGC 2903, and NGC 3310).

Table 7 lists for each region in columns 1 to 5: (1) the region ID; (2) the number of stellar knots present in the region; (3) the mean radius in pc; (4) the dynamical mass in M_{\odot} ; and (5) the ratio of ionising to dynamical mass. To calculate this ratio, we used the ionising masses calculated in the first paper of the series from the number of hydrogen ionising photons, $Q(H\alpha)$, and the equivalent width of the $H\beta$ emission line to take into account the cluster evolution. We used a Salpeter IMF $\phi(m) = m^{-\alpha}$, with $\alpha = 2.35$, $m_{low}(M_{\odot}) = 0.85$, and $m_{up}(M_{\odot}) = 120$, which seems the most suitable for the age of our regions.

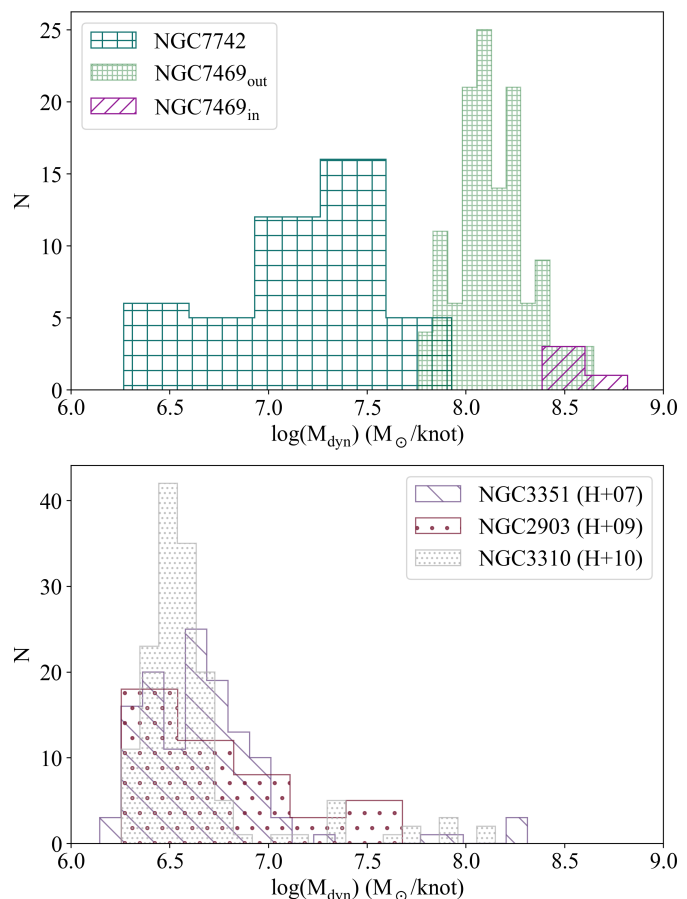


Fig. 10. Distributions of the dynamical masses of each knot for the CNSFRs. The top panel shows the results in this work and the outer and inner ring regions of NGC 7469. The bottom panel shows data from the literature (Hägele et al. 2010, 2007, 2009, labelled (H+07), (H+09), and (H+10) respectively).

Figure 11 shows the distribution of the calculated dynamical masses for each CNSFR. The dynamical masses of inner and outer ring regions of NGC 7469, calculated in the second paper of this series are also shown. Additionally, we show the masses of CNSFRs reported in the literature for NGC 3351, NGC 2903, and NGC 3310, which were calculated with the same method described in this work (Hägele et al. 2010, 2007, 2009). The dynamical masses of NGC 7742 clusters range from 2.5×10^6 to $1.0 \times 10^8 M_{\odot}$, values similar to those found in the rest of the galaxies shown, but lower than those obtained for the two rings of NGC 7469.

The ratio of ionising to dynamical masses has values ranging from 0.15 to 7.07 %, implying a contribution by recent star formation for the ring regions larger than found in other galaxies. For comparison, this percentage ranges from 0.02 to 0.91 % for the CNSFRs in the outer ring of NGC 7469 whose distance to the galactic nucleus is similar to that of the NGC 7742 ring to its nucleus.

4.3. Kinematics of stars and ionised gas

In Sect. 3.2 we derive the radial velocities and velocity dispersions of the ionised gas in the apertures of the selected HII regions. Our results suggest the existence of at least two kinematically distinct $H\alpha$ components that can be identified in the spectra of CNSFRs

Table 7. Stellar cluster masses and sizes for observed CNSFRs.

Region ID	N_{knots}	R_{mean}^* (pc/knot)	M_{dyn} (M_{\odot})	M_{ion}/M_{dyn} (per cent)
R1	1	13.9	$(6.2 \pm 3.6) \times 10^6$	2.57
R3	2	15.0	$(25.9 \pm 2.7) \times 10^6$	1.47
R5	1	16.3	$(84.6 \pm 3.0) \times 10^6$	0.15
R7	1	9.9	$(3.5 \pm 1.5) \times 10^6$	6.61
R8	1	20.1	$(2.5 \pm 2.6) \times 10^7$	1.32
R14	2	12.8	$(8.3 \pm 2.0) \times 10^6$	2.20
R15	1	12.1	$(8.2 \pm 3.9) \times 10^6$	1.45
R16	1	10.1	$(22.8 \pm 3.6) \times 10^6$	2.26
R22	1	10.1	$(12.2 \pm 6.5) \times 10^6$	2.24
R23	2	14.6	$(38.3 \pm 8.6) \times 10^6$	0.73
R26	2	14.6	$(9.5 \pm 2.3) \times 10^6$	3.00
R31	4	10.1	$(74.4 \pm 7.6) \times 10^6$	0.40
R33	1	15.2	$(30.2 \pm 6.8) \times 10^6$	0.77
R36	1	10.6	$(481.8 \pm 6.6) \times 10^5$	0.77
R41	3	14.8	$(100.4 \pm 6.7) \times 10^6$	0.59
R45	2	18.1	$(10.0 \pm 2.3) \times 10^7$	0.19
R47	2	12.2	$(3.2 \pm 1.1) \times 10^7$	0.55
R50	1	10.1	$(17.6 \pm 3.9) \times 10^6$	1.21
R51	1	71.3	$(8.4 \pm 3.1) \times 10^7$	0.39
R52	3	14.9	$(31.4 \pm 4.9) \times 10^6$	1.46
R53	1	10.1	$(22.6 \pm 1.0) \times 10^6$	0.58
R55	3	14.1	$(73.4 \pm 6.7) \times 10^6$	0.13
R57	2	14.7	$(5.4 \pm 1.1) \times 10^6$	7.07
R60	1	13.1	$(12.7 \pm 5.8) \times 10^6$	0.90
R63	1	10.1	$(9.6 \pm 4.3) \times 10^6$	1.33
R69	1	14.4	$(2.5 \pm 2.4) \times 10^6$	4.16
R74	1	19.2	$(9.3 \pm 4.6) \times 10^6$	1.14

with high S/N. We compared their radial velocities in order to find out which of them are associated with the ionising clusters.

The left panel of Fig. 12 shows the comparison of the velocities of the $H\alpha$ broad and narrow components with the one-to-one line represented by a dashed grey line. We can see that the two radial velocities coincide within the errors. Only two regions seem to fall off the one-to-one line: R62, and R65. An additional component of the $H\alpha$ emission line has been identified in seven of the regions, and a comparison of their velocities and those of the narrow component is shown in the right panel of the same figure. Only three of these additional components, in regions R1, R7, and R67, seem to be associated with the ionising clusters, and hence they can be attributed to local effects inside the regions. In the other four cases, that component may have an external origin.

The left panels of Fig. 13 show the gas velocity of the narrow component of forbidden emission lines as a function of the corresponding $H\alpha$ component. Results for the [NII] λ 6584 Å, [SII] λ 6731 Å, and [SIII] λ 9532 Å emission lines are shown from top to bottom. All regions follow the one-to-one relation within the errors, hence assuring that the selected kinematical components are associated with the observed HII regions. Only in the case of the [SIII] emission line do a few regions seem to deviate from the identity relation; these regions show large observational errors related to low S/N spectra. The right panels of the figure show the same relations, but for the broad-line component of both forbidden and $H\alpha$ lines. All the [NII] broad components follow the one-to-one relation; their association with the observed HII regions is guaranteed. For the [SII] lines, only in three of the regions is the presence of a broad component consistent with the

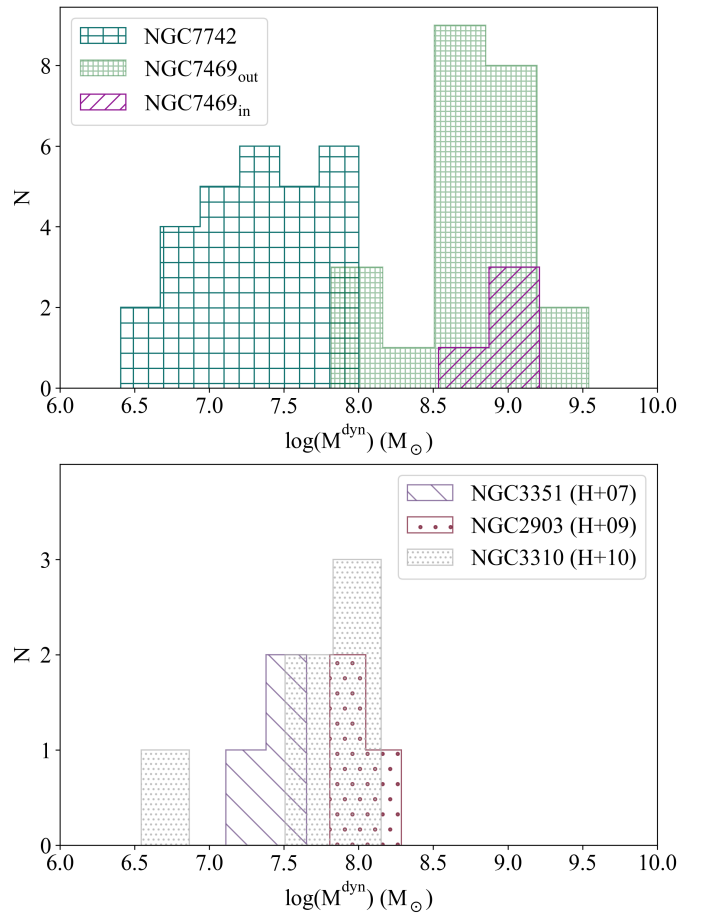


Fig. 11. Histograms of the distribution of dynamical masses for the CNSFRs in this work, the outer and inner ring regions of NGC 7469, and data from the literature as labelled (Hägele et al. 2010, 2007, 2009, (H+07), (H+09), and (H+10) respectively).

S/N, and only one region shows a broad component in the [SIII] emission lines; this region, R1, displays complex kinematics with three different width velocity components, clearly identified in the $H\alpha$ and [NII] λ 6548,84 Å lines, that seem to be associated with the HII region (see Fig. 3).

Figure 14 shows the comparison between the derived velocity dispersion for stars and gas in the selected CNSFRs. Gas narrow and broad components are represented by blue dots and green triangles, respectively, while regions showing a single component are represented by purple squares. The dashed grey line shows the one-to-one relation. The top left panel of this figure shows the results for the $H\alpha$ emission line. We can see that the narrow components have velocity dispersions lower than the stellar values and in a narrow range with a mean value of $\overline{\sigma}_{H\alpha} = 9.26$ km/s, shown by a red solid line; the dotted red lines represent the standard deviation of the distribution. Regions that have only one component show a similar behaviour. On the other hand, the broad components lie slightly above the one-to-one relation in regions with low star velocity dispersions. This behaviour seems to be lost for higher values of σ_{CaT} . The top right panel of the figure shows the results for [NII], which show the same behaviour as the $H\alpha$ line. In this case, the mean velocity dispersion of the narrow component is $\overline{\sigma}_{[NII]} = 11.2$ km/s and the standard deviation is slightly larger. For the broad component the same trend seen for the $H\alpha$ line is easily recognizable. The only component identified in the [SII] lines, shows the same velocity dispersion associated

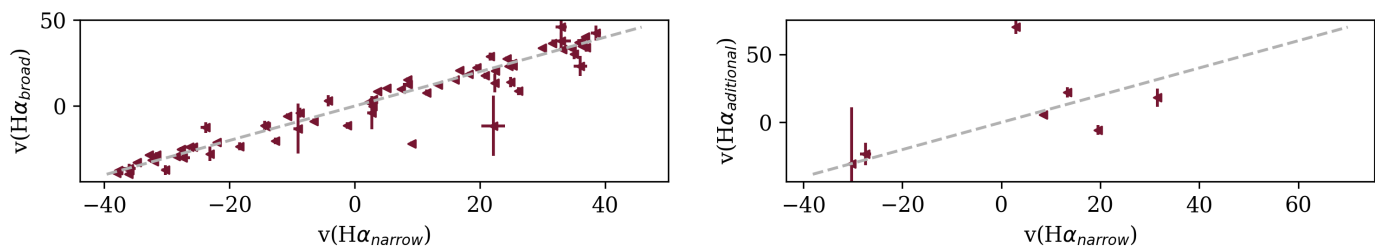


Fig. 12. Velocity of different components of H α measured in each region. The narrow component velocity is shown against the broad and additional components, in the left and right panels, respectively. All velocities are shown in km/s.

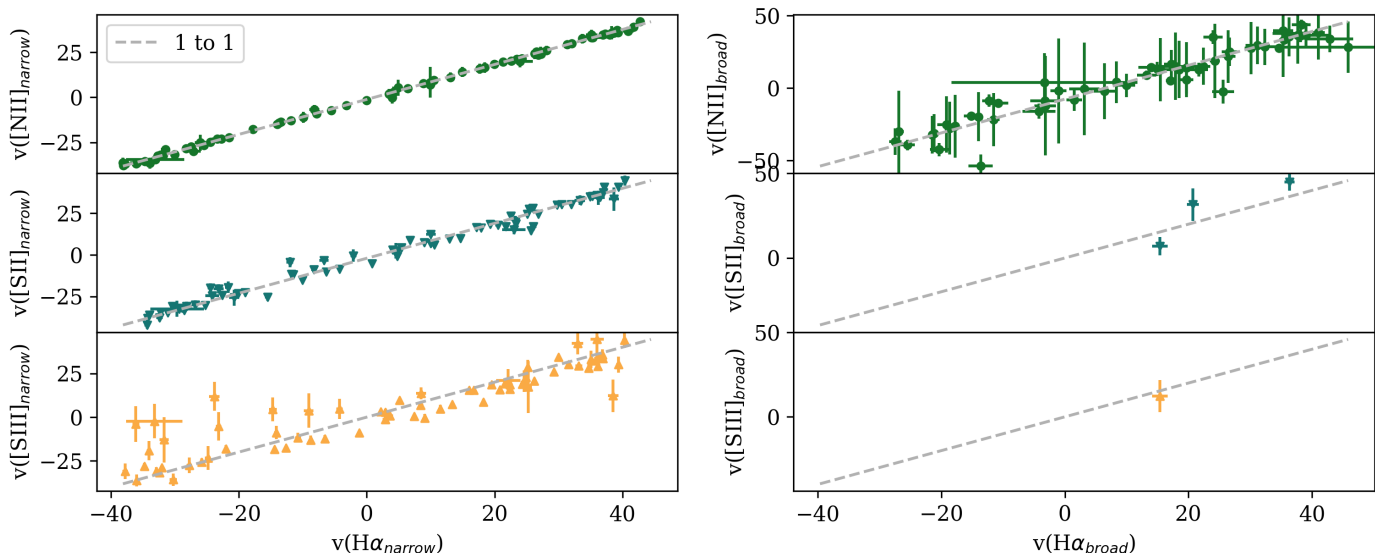


Fig. 13. Comparison of the radial velocity of the different measured components of the [NII], [SII], and [SIII] lines in each region (from top to bottom) with those of the narrow and broad H α components (left and right panels). All velocities are shown in km/s.

with the gas narrow component, showing a mean value of $\bar{\sigma}_{[SII]} = 15.8$ km/s (see the lower right panel of the figure), while for the [SIII] lines the velocity dispersions show a more complex behaviour, as shown in the lower right panel of the figure; the single component present shows a wider velocity dispersion distribution, although mostly below the one-to-one line. The only region with a broad component in [SIII] is R1 appearing in the top left corner of the diagram, with a gas velocity dispersion of 65 km/s (this region is close to supernova SN 1993R).

Similar results to those presented above have also been found in other extragalactic HII region studies in the literature. For example in Firpo et al. (2010), where some giant HII regions in the NGC 7479 spiral galaxy were analysed using echelle spectroscopy data with a similar spectral resolution to that of MEGARA. In this work, region III is reported to show a broad Gaussian component in the H α and [NII] emission lines with a velocity dispersion in the range between 37.8 km/s and 51.2 km/s, while the narrow component is around 10 km/s and no broad component was found in the [OIII] profile whose velocity profile can be fitted with a Gaussian with a value of σ around 20 km/s. In addition, CNSFRs of different galaxies studied in Hägele et al. (2009, 2010) show broad components in the emission lines at the same radial velocity as the narrow ones within the errors; the authors identified the narrow and broad components with ionised gas supported by rotation and dynamical pressure respectively. Interestingly, the CNSFR rings in both galaxies are thought to have been produced in a minor merger event.

A diversity of line broadening mechanisms have been proposed to explain the line profiles of HII regions. Winds associated with WR stars or young main sequence O stars (i. e. Diaz et al. 1987; Terlevich et al. 1996) could produce them. However, the expected broadening due to WR winds would, in general, be greater than observed in our clusters since these stars can have winds of thousands of km/s. On the other hand, we estimated the number of O stars that may be present in the CNSFRs of this study. To do so we used the Salpeter (1955, $m_{low} = 0.85M_{\odot}$, $m_{up} = 120 M_{\odot}$) IMF and models from (Smith et al. 2002, Z_{\odot} , $\log(g) = 4$, $R^* = 7.1 - 10.6 R_{\odot}$), which derive the following equation:

$$N_O = 6.437 \cdot 10^{-5} M_{cluster}. \quad (5)$$

Here $M_{cluster}$ is expressed in solar masses. For the clusters with derived dynamical mass this number is between 1 and 38, with a mean value of ~ 10 stars. However, normal O stars have winds with velocities $\sim 10^3$ km/s, depending on the density of the environment. Thus, they would also provide a broadening larger than observed. In conclusion, we rule out stellar winds as the main broadening mechanism in our CNSFRs.

A second alternative could be related to the interaction of the hot phase of the ISM with cooler gas knots forming a turbulent mixing layer with velocities of about 100 to 400 km/s (Westmoquette et al. 2007b,a); Champagne flows arising from the photo-erosion of denser clumps of gas also would produce velocities larger than observed although they can contribute to the turbulence of the ISM (Tenorio-Tagle et al. 1985).

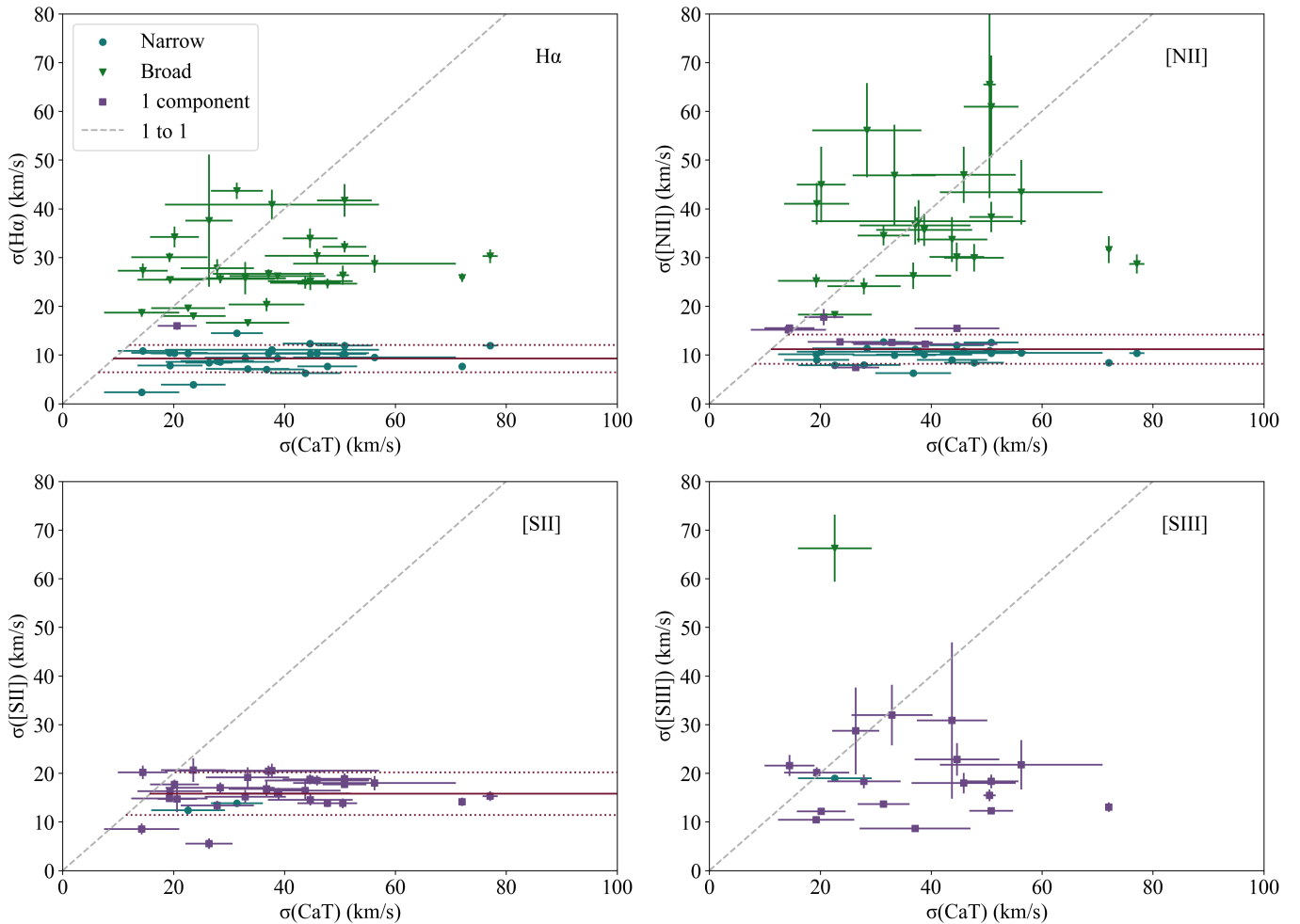


Fig. 14. Relation between the velocity dispersion of stars (CaT) and ionised gas ($H\alpha$, $[NII]\lambda 6584 \text{ \AA}$, $[SII]\lambda 6731 \text{ \AA}$, and $[SIII]\lambda 9532 \text{ \AA}$ emission lines) for the selected CNSFRs. The red horizontal solid line represents the average velocity dispersion of the gas narrow component; the dashed red lines correspond to the $\pm 1 \sigma$ value.

Another possible explanation proposed in the literature is the turbulence of the interstellar gas. In 1994, Chu & Kennicutt (1994) studied the 30 Doradus giant HII region, in the Large Magellanic Cloud. The outer regions of the nebula have a smooth turbulent velocity field with velocities of 13 to 17 km/s and, at the central regions, the velocity is dominated by multiple expanding structures from 8.5 to 85 km/s (in units of σ). They corroborated that the integration of all these structures produced a simple broad Gaussian profile with faint extended wings. Additionally, several fast expanding shells were found with velocities from ~ 40 to 130 km/s. (Medina Tanco et al. 1997) studied the giant HII region NGC 604, in M33 finding structure in the velocity field projected along the line of sight that could be attributed to turbulence and suggesting that this turbulence could be powered by recent star formation processes. According to this, the broad component of velocity dispersions found in our particular case look similar to those produced by interstellar gas turbulence.

However, the works just mentioned above lack the information related to the comparison between gas and stars velocity dispersions, and this fact provides additional important information: the stars and the gas associated with the broad component of the emission lines showing similar values of velocity dispersion, and sharing a common kinematics, can be explained if they respond to the same gravitational potential of the cluster. From the results obtained in the first paper in this series, we concluded that

ring clusters are composed of a young non-ionising intermediate age population about 300 Ma old, plus an ionising population of 4.7 Ma in a 4:1 ratio. In this scenario, the ring clusters would have formed almost simultaneously in a first star formation episode. The stars in such a population would return part of their gas to the interstellar medium during their evolution. A fraction of this gas could escape from the cluster, while some of it would be unable to do so thus remaining trapped in the cluster (Silich & Tenorio-Tagle 2018). This gas would feel the same gravitational potential as the cluster stars, consistent with our results. A fraction of the gas that cooled down would form a new stellar population, which would be responsible for the ionising photons. In this scenario, the narrow gas component would be associated with the HII region ionisation shell. According to the results presented here (see Sect. 4.2, this young ionising stellar population accounts for between 0.15 and 7.07 % of the total dynamical mass of the cluster.

5. Conclusions

In this third paper in the series, we analysed the kinematics of gas and stars in the circumnuclear ring of NGC 7742 estimating the dynamical masses of their CNSFRs from high spectral resolution data. We extracted spectra for each region using the apertures selected from $H\alpha$ images. The analysis of the emis-

sion line profiles, show the presence of two different kinematical components with the same radial velocity. These two different components were found in the H α emission line in $\sim 90\%$ of the analysed regions; most of them also showed the same component in the [NII] emission lines. The narrow component has an almost constant value between 10 km/s and 15 km/s, while the broad component velocities are between 20 and 45 km/s.

In spite of the contribution to the nebular continuum, the CaT lines are seen almost undiluted pointing to the stellar population being dominated by red giant or supergiant stars.

The sizes of the star clusters were measured from a F555W WFPC2-HST image. About $\sim 60\%$ show a single star-forming knot; the rest of them show between two and four knots each. Cluster velocity dispersions were derived from the CaT absorption lines using a modified version of the Tonry & Davis cross-correlation technique. These velocities together with the measured sizes were used to calculate the cluster dynamical masses under the assumption that the clusters are virialised. The masses were found to be between 2.5×10^6 and $1.0 \times 10^8 M_{\odot}$, values similar to those found in the literature for circumnuclear clusters.

Finally, a comparison of the gas and star velocity dispersion, seldom found in the literature, was made revealing a complex internal structure of the gas. A scenario was put forward suggesting that the circumnuclear ring clusters formed simultaneously in a first star formation episode whose high-mass stars could have returned part of their gas to the interstellar medium during their evolution. A fraction of this initial ejecta remained trapped in the gravitational potential of the cluster. A fraction of the trapped gas cooled down and formed the young stellar population responsible for the ionisation of the gas currently observed. This young stellar population accounts for between 0.15 and 7.07% of the total dynamical mass of the cluster.

Acknowledgements. This research has made use of the services of the ESO Science Archive Facility and NASA's Astrophysics Data System Abstract Service. It is based on observations collected at the European Organisation for Astronomical Research in the Southern Hemisphere under ESO programme 60.A-9301(A) and data products created thereof. Also we have used observations obtained with the NASA/ESA HST and also from the *Hubble* Legacy Archive, which is a collaboration between the Space Telescope Science Institute (STScI/NASA), the Space Telescope European Coordinating Facility (ST-ECF/ESA), and the Canadian Astronomy Data Centre (CADC/NRC/CSA). This work has been supported by Spanish grants from the former Ministry of Economy, Industry and Competitiveness through the MINECO-FEDER research grants AYA2016-79724-C4-1-P, and PID2019-107408GB-C42 and the present Ministry of Science and Innovation through the research grant PID2022-136598NB-C33 by MCIN/AEI/10.13039/501100011033 and by "ERDF A way of making Europe". S.Z. acknowledges the support from contract: BES-2017-080509 associated with the first of these grants. This work is based on observations made with the Gran Telescopio Canarias (GTC), installed at the Spanish Observatorio del Roque de los Muchachos of the Instituto de Astrofísica de Canarias, on the island of La Palma. The data was obtained with the instrument MEGARA funded by European Regional Development Funds (ERDF), through Programa Operativo Canarias FEDER 2014–2020.

References

Böker, T., Falcón-Barroso, J., Schinnerer, E., Knapen, J. H., & Ryder, S. 2008, *AJ*, 135, 479
 Brandl, B. R., Martín-Hernández, N. L., Schaerer, D., Rosenberg, M., & van der Werf, P. P. 2012, *A&A*, 543, A61
 Cardiel, N. & Pascual, S. 2018, *guaix-ucm/megaradp-calibrations: Release 2018.1*, Zenodo
 Carrasco, E., Gil de Paz, A., Gallego, J., et al. 2018, in *Society of Photo-Optical Instrumentation Engineers (SPIE) Conference Series*, Vol. 10702, *Ground-based and Airborne Instrumentation for Astronomy VII*, ed. C. J. Evans, L. Simard, & H. Takami, 1070216
 Chu, Y.-H. & Kennicutt, Robert C., J. 1994, *ApJ*, 425, 720
 de Zeeuw, P. T., Bureau, M., Emsellem, E., et al. 2002, *MNRAS*, 329, 513

Díaz, Á. I., Terlevich, E., Castellanos, M., & Hägele, G. F. 2007, *MNRAS*, 382, 251
 Diaz, A. I., Terlevich, E., Pagel, B. E. J., Vilchez, J. M., & Edmunds, M. G. 1987, *MNRAS*, 226, 19
 Fernández, V., Amorín, R., Sanchez-Janssen Macarena Garcia del Valle-Espinosa, R., & Papaderos, P. 2022, *arXiv e-prints*, arXiv:2212.10593
 Firpo, V., Bosch, G., Hägele, G. F., & Morrell, N. 2010, *MNRAS*, 406, 1094
 García-Vargas, M. L., Carrasco, E., Mollá, M., et al. 2020, *MNRAS*, 493, 871
 Garcia Vargas, M. L., Diaz, A. I., Terlevich, E., & Terlevich, R. 1993, *Ap&SS*, 205, 85
 Hägele, G. F., Díaz, Á. I., Cardaci, M. V., Terlevich, E., & Terlevich, R. 2007, *MNRAS*, 378, 163
 Hägele, G. F., Díaz, Á. I., Cardaci, M. V., Terlevich, E., & Terlevich, R. 2009, *MNRAS*, 396, 2295
 Hägele, G. F., Díaz, Á. I., Cardaci, M. V., Terlevich, E., & Terlevich, R. 2010, *MNRAS*, 402, 1005
 Hägele, G. F., Díaz, Á. I., Terlevich, R., et al. 2013, *MNRAS*, 432, 810
 Ho, L. C. & Filippenko, A. V. 1996a, *ApJ*, 466, L83
 Ho, L. C. & Filippenko, A. V. 1996b, *ApJ*, 472, 600
 Keel, W. C. 1983, *ApJ*, 269, 466
 Kennicutt, Robert C., J., Keel, W. C., & Blaha, C. A. 1989, *AJ*, 97, 1022
 Knapen, J. H. 2005, *A&A*, 429, 141
 Levy, R. C., Bolatto, A. D., Leroy, A. K., et al. 2022, *ApJ*, 935, 19
 Lopez, S., Lopez, L. A., Nguyen, D. D., et al. 2023, *ApJ*, 942, 108
 Mazzuca, L. M., Knapen, J. H., Veilleux, S., & Regan, M. W. 2008, *ApJS*, 174, 337
 Medina Tanco, G. A., Sabalisk, N., Jatenco-Pereira, V., & Opher, R. 1997, *ApJ*, 487, 163
 Mollá, M., García-Vargas, M. L., & Bressan, A. 2009, *MNRAS*, 398, 451
 Oliva, E., Origlià, L., Kotilainen, J. K., & Moorwood, A. F. M. 1995, *A&A*, 301, 55
 Pascual, S., Cardiel, N., Picazo-Sanchez, P., Castillo-Morales, A., & Gil de Paz, A. 2018, *guaix-ucm/megaradp: v0.8*, Zenodo
 Pizzella, A., Corsini, E. M., Vega Beltrán, J. C., & Bertola, F. 2004, *A&A*, 424, 447
 Salpeter, E. E. 1955, *ApJ*, 121, 161
 Sarzi, M., Allard, E. L., Knapen, J. H., & Mazzuca, L. M. 2007, *MNRAS*, 380, 949
 Silich, S. & Tenorio-Tagle, G. 2018, *MNRAS*, 478, 5112
 Skrutskie, M. F., Cutri, R. M., Stiening, R., et al. 2006, *AJ*, 131, 1163
 Smith, L. J., Norris, R. P. F., & Crowther, P. A. 2002, *MNRAS*, 337, 1309
 Tenorio-Tagle, G., Bodenheimer, P., & Yorke, H. W. 1985, *A&A*, 145, 70
 Terlevich, E., Diaz, A. I., & Terlevich, R. 1990, *MNRAS*, 242, 271
 Terlevich, E., Díaz, A. I., Terlevich, R., et al. 1996, *MNRAS*, 279, 1219
 Tonry, J. & Davis, M. 1979, *AJ*, 84, 1511
 Westmoquette, M. S., Smith, L. J., Gallagher, J. S., I., et al. 2007a, *ApJ*, 671, 358
 Westmoquette, M. S., Smith, L. J., Gallagher, J. S., & Exter, K. M. 2007b, *MNRAS*, 381, 913
 Zamora, S. & Díaz, Á. I. 2023a, *arXiv e-prints*, arXiv:2310.12895
 Zamora, S. & Díaz, Á. I. 2023b, *MNRAS*, 525, 5767
 Zamora, S. & Díaz, Á. I. 2023c, *arXiv e-prints*, arXiv:2310.04133